RSC Advances

PAPER

View Article Online
View Journal | View Issue

Cite this: *RSC Adv.*, 2016, **6**, 104359

Controlled growth of organic–inorganic hybrid $CH_3NH_3PbI_3$ perovskite thin films from phase-controlled crystalline powders†

Yong Chan Choi,* Se Won Lee, Hyo Jeong Jo, Dae-Hwan Kim and Shi-Joon Sung*

Received 29th July 2016
Accepted 25th October 2016

DOI: 10.1039/c6ra19203c

www.rsc.org/advances

High-quality $CH_3NH_3PbI_3$ ($MAPbI_3$) crystalline powders were synthesized from a dispersion of $MAPbI_3$ solution (solvent: *N*,*N*-dimethylformamide (DMF)) in the antisolvent dichloromethane. They were used as starting chemicals for precursor solutions. The PbI_2–DMF-, perovskite-, and PbI_2–MAI (methylammonium iodide)–DMF-dominant phases were preferentially formed under conditions of excess PbI_2, moderate, and high-excess MAI input ratios, respectively. The input ratio of powders in fabricating the thin $MAPbI_3$ films strongly affected not only the morphology and structure of the films, but also the photovoltaic performance of the devices using them. The devices were constructed as follows: Au/hole-transporting material/$MAPbI_3$/mesoporous TiO_2 layer/TiO_2 blocking layer/F-doped SnO_2. The best device performance was obtained from the powder with a specific ratio of PbI_2 : MAI = 1 : 1.6; the device exhibited a power conversion efficiency of ~16% at 1.5G standard conditions. Our proposed method could provide a simple and versatile solution-based approach for a low-cost perovskite solar cell fabrication technology.

1. Introduction

Organic–inorganic hybrid perovskites, such as $CH_3NH_3PbX_3$ (methylammonium PbX_3 or $MAPbX_3$), $HC(NH_2)_2PbX_3$ (formamidinium PbX_3 or $FAPbX_3$), (FA,MA)PbX_3, and (FA,Cs)PbX_3 (X = I, Br, and Cl), are considered to be among the most promising photovoltaic materials owing to their peculiar optical and electrical properties and remarkable improvements in device performance within the past several years.[1–5] Very recently, the certified power conversion efficiency (PCE) of such devices fabricated by Seok *et al.* exceeded 20%.[2] This efficiency is comparable to those of commercially available inorganic solar cells based on CdTe and Si. Hybrid perovskite photovoltaic devices can be readily fabricated on flexible substrates at low temperatures,[6] which shows high potential for realizing low-cost photovoltaic systems. However, hybrid perovskite solar cells remain inadequate for commercialization because of several critical issues, such as material instability,[6,7] Pb-induced toxicity,[8] photocurrent hysteresis,[1,9,10] interfacial problems,[7,11] low flexibility,[6] and scale-up issues.[6]

Along with research efforts to meet the standards for low-cost industrial production, many researchers have attempted to improve the current solution-processing approach used to fabricate hybrid perovskites with high crystallinity, stability, uniformity, and reliable reproducibility.[1,12–19] Initially, hybrid perovskites films suffered from low surface-coverage and crystallinity, limiting the PCE enhancement. To address this issue, some researchers focused on the modification of the precursor solutions used for one-step solution methods. Additional chemicals, such as halides,[13–15] PbI_2/$PbCl_2$,[15,16] and solvent additives,[14,17] have been applied to the precursor solution to improve the morphology and crystallinity of the resulting thin films. Efforts were also made to replace the typical lead precursors of PbI_2 and $PbCl_2$ with $Pb(CH_3COO)_2$ (ref. 18) to control the crystal growth kinetics. Alternatively, several groups addressed the morphology problems by solvent- or complex-engineering. Jeon *et al.* first introduced a solvent-engineering technique consisting of intermediate-phase formation and the rapid stabilization of the intermediate phase by drip-casting with toluene.[1] The prepared $MAPbI_{3-x}Br_3$ films exhibited uniform morphology and excellent photovoltaic performance without photocurrent hysteresis. Ahn *et al.* improved this technique by controlling the intermediate phase formation and using diethyl ether as a dripping-solvent instead of toluene.[19] However, these solution methods entail common drawbacks. The quality of the final product strongly depends on the purity and hydration of the starting chemicals.[20–22] Frequently, different methods must be applied depending on the type of hybrid perovskite being produced. For example, a modified two-step solution method, the so-called intramolecular exchange method, must be adopted for fabricating uniform and pinhole-free $FAPbI_3$ because fabricating such high-quality

Convergence Research Center for Solar Energy, Daegu Gyeongbuk Institute of Science & Technology (DGIST), Daegu 42988, Republic of Korea. E-mail: ycchoi@dgist.ac.kr; sjsung@dgist.ac.kr

† Electronic supplementary information (ESI) available. See DOI: 10.1039/c6ra19203c

$FAPbI_3$ thin films is quite difficult using solvent-engineering techniques.[2] Therefore, it remains a challenge to develop a simple, versatile, and generic solution-based approach for the fabrication of various hybrid perovskites.

Recently, Shi *et al.* reported interesting results for the single-crystal growth of $MAPbX_3$ using an antisolvent vapor-assisted crystallization (AVC) technique.[23] The single crystals were grown very slowly by the vapor-phase diffusion of the anti-solvent into $MAPbX_3$ precursor solutions. Dichloromethane (DCM) was used as the antisolvent because it interacts very poorly with MAX and PbX_2. Through this method, they successfully fabricated high-quality $MAPbX_3$ single crystals with low trap density and long carrier diffusion length. This excellent study inspired us to develop a simple solution approach.

We initially attempted to use high-quality $MAPbI_3$ crystals synthesized by the AVC technique as the starting chemicals for the precursor solutions. However, direct use of such crystals is impractical because the original AVC method requires weeks to obtain high-quality single crystals.[23] Therefore, we modified the method to reduce the time necessary for crystal growth. We directly dispersed a solution of $MAPbI_3$ in DCM antisolvent, instead of using slow vapor-phase diffusion of DCM. This modified procedure allowed us to rapidly obtain high-quality $MAPbI_3$ crystalline powders. In addition, we chose *N*,*N*-dimethylformamide (DMF) to synthesize the $MAPbI_3$ solution, rather than γ-butyrolactone (GBL), to control the powder phases because powders with variable phases could not be obtained from the solution dissolved in GBL (Fig. S1†). As a result, through this method, we could simply control the formed powder phases, as well as the morphology and structure of the final products, by tuning the input molar ratio of the precursor.

In this work, we introduce a simple and versatile solution method using $MAPbI_3$ crystalline powders, synthesized by the modified AVC technique, for the fabrication of high-performance $MAPbI_3$ perovskite solar cells. The $MAPbI_3$ powders are simply obtained by dispersing $MAPbI_3$ solutions in DMF with various molar ratios of PbI_2/MAI in DCM antisolvent. The synthesized powders exhibit the three phases of PbI_2–DMF, perovskite, and PbI_2–MAI–DMF; the dominant phase can be controlled by tuning the ratio of PbI_2 to MAI. In addition, the performance of devices based on films from these powders is strongly dependent on the powder type. The highest PCE of ~16%, without a significant photocurrent hysteresis, is obtained from the powder with a specific ratio of PbI_2 : MAI = 1 : 1.6.

2. Results and discussion

Fig. 1 illustrates the experimental procedure for the $MAPbI_3$ powder synthesis. First, $MAPbI_3$ solutions are formed by dissolving PbI_2 and MAI at various molar ratios of PbI_2 : MAI = 1 : 0.7–2.2 in DMF (step I). After the clear yellowish solutions are obtained, the solutions are loaded into plastic syringes and dispersed in the DCM antisolvent (step II). When the solutions are released from the syringes, black and white precipitates are immediately formed within the DCM, as shown in the photographs of step II of Fig. 1 and S2.† Notably, the amount of black precipitate is rapidly increased with an abrupt decrease of white as the ratio of MAI/PbI_2 is increased. The precipitates are collected by vacuum filtration, washed several times with DCM, and dried for several days in vacuum at room temperature to remove DCM from the precipitates. Finally, they are ground to fine powders and stored in a desiccator for use as chemical sources for the precursor solutions and material analysis (step III). As shown in the photograph of step III, as the MAI ratio increases from PbI_2 : MAI = 1 : 0.7 to 1 : 1.6, the color of powders is changed from light gray to black. However, with further increases in the MAI ratio, the powder becomes lighter (dark gray, 1 : 1.9) and turns pink (1 : 2.2). The different colors of the as-prepared powders suggest the formation of different phases depending on the input ratio. We also observe that the volume of obtained powder is gradually increased with increases in the MAI ratio, despite the samples having the same weight, as shown in the photograph of step III.

In order to apply the synthesized powders in solar cells, we fabricated devices composed of Au/hole-transporting material (HTM)/$MAPbI_3$/mesoporous TiO_2 (mp-TiO_2)/TiO_2 blocking layer (TiO_2–BL)/F-doped SnO_2 (FTO, TEC-8). To minimize the current density–voltage (*J*–*V*) hysteresis phenomena depending on measurement conditions, we varied the mp-TiO_2 thickness from 150 to 1000 nm, as proposed by Jeon *et al.*,[1] and deposited thin mp-TiO_2 layers of ~200 nm in thickness. The $MAPbI_3$ was deposited by spin-coating solutions of ~45 wt% powders in DMF with a solvent dripping technique[1,19] before annealing at 120 °C for 15 min in air. Spiro-OMeTAD (2,2′,7,7′-tetrakis(*N*,*N*-dimethoxyphenylamine)-9,9′-spirobifluorene) was used as HTM. Fig. 2a and b show the effects of the input PbI_2 : MAI ratio on the photovoltaic device performance. The photovoltaic parameters are summarized in Table 1. As the MAI ratio is

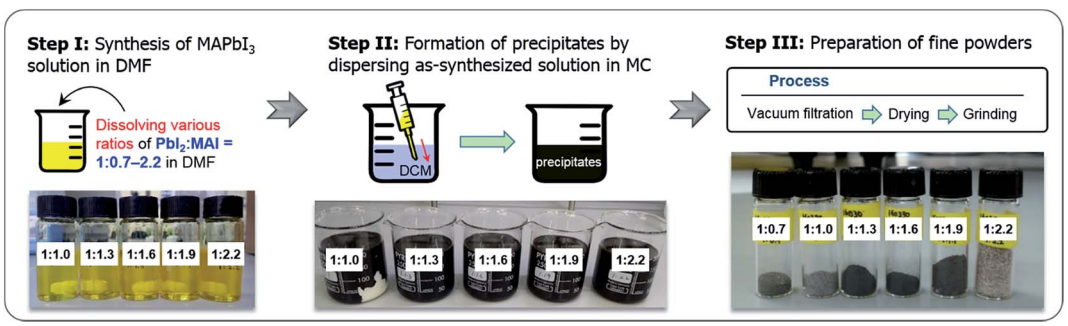

Fig. 1 Schematics and corresponding photographs of the experimental process for synthesizing $MAPbI_3$ powders.

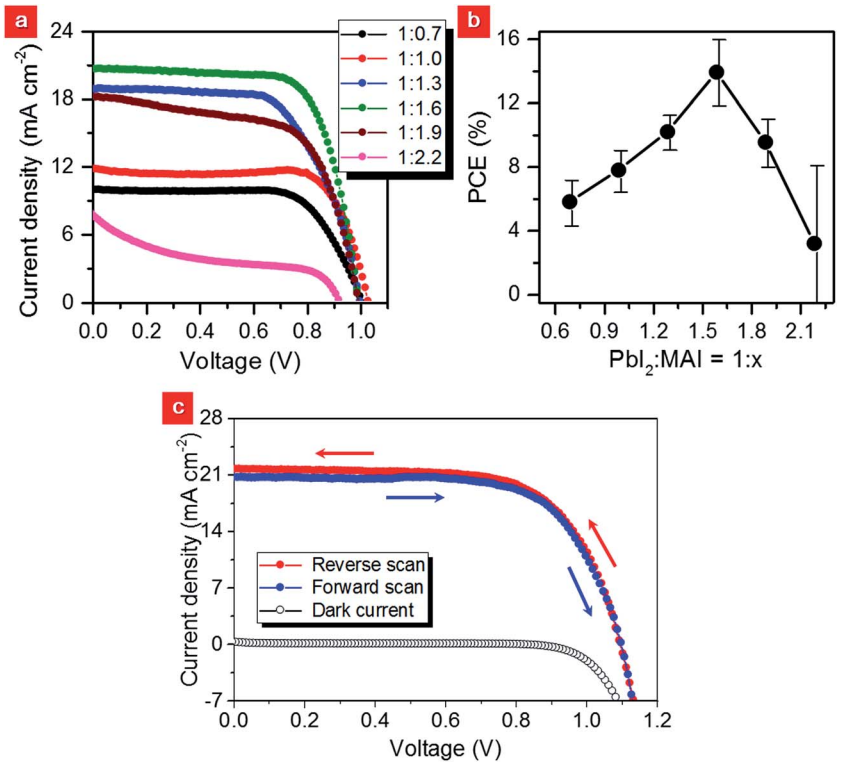

Fig. 2 Photovoltaic device performances with different PbI_2 : MAI ratios: (a) typical *J–V* curves and (b) PCE graph. The curves of (a) were obtained in reverse scan mode; (b) was obtained from the *J–V* curves of 60 devices. (c) *J–V* curves of the best-performing device fabricated with the 1 : 1.6 powder. All curves were obtained with a sweep delay time of 100 ms and a voltage step value of 0.01 V under standard AM 1.5G illumination.

increased from 1 : 0.7 to 1 : 1.6, the PCE is gradually increased from 6.9 (average value: 5.7 ± 1.4) to 14.3 (average value: 13.9 ± 2.1)% because of the enhanced short-circuit current density (J_{SC}). However, further increase in the MAI ratio causes all parameters to decrease, thereby decreasing the PCE. In particular, the device fabricated with the 1 : 2.2 powder exhibits highly unstable performance. These results indicate an optimum input ratio of 1 : 1.6 for powders to promote good device performance. Through this optimization, we obtain the highest PCE of ~16.0% in the reverse-scan mode, with a J_{SC} of 21.1 mA cm^{-2}, an open-circuit voltage (V_{OC}) of 1100.2 mV, and a fill factor (FF) of 68.9%, from the samples fabricated with the powder formed by a 1 : 1.6 input ratio (Fig. 2c and Table 2). The *J–V* curves between the reverse and forward scans also exhibit very little hysteresis.

To elucidate the effects of the input PbI_2 : MAI ratio on the device performance, we investigated the structures and compositions of the prepared powders. Fig. 3a shows the X-ray diffraction (XRD) patterns of the prepared powders prepared from different PbI_2 : MAI input ratios. The patterns of pure PbI_2 and MAI are shown for comparison. Based on careful examination and comparison with previous reports, we identify the three main phases of a PbI_2–DMF complex,[24] PbI_2–MAI–DMF complex,[24] and a tetragonal-type perovskite.[23,24] These three phases are denoted by green triangles, blue diamonds, and red circles in Fig. 3a, respectively. In addition to these phases, the MAI phase (brown stars) is observed from the powder of 1 : 2.2. To analyze the phase percentage quantitatively from the XRD patterns, we first defined the three phases of PbI_2–DMF complex, tetragonal perovskite, and PbI_2–MAI–DMF complex, and compared them with XRD patterns, as shown in Table S1,† based on crystal structure parameters previously reported by Guo *et al.*[24] Then, we analyzed the phase ratio using the Rietveld method, as plotted in Fig. 3b. As shown in Fig. 3a and b, the PbI_2–DMF complex phase is dominant at the ratio of 1 : 0.7, but

Table 1 Summary of device parameters shown in Fig. 2a

PbI_2 : MAI	J_{SC} (mA cm^{-2})	V_{OC} (mV)	FF (%)	PCE (%)
1 : 0.7	9.9	1007.1	68.8	6.9
1 : 1.0	11.8	1030.2	75.2	9.1
1 : 1.3	18.9	1000.1	61.7	11.7
1 : 1.6	20.7	995.4	69.4	14.3
1 : 1.9	18.2	995.3	61.6	11.2
1 : 2.2	7.6	922.3	17.5	1.2

Table 2 Summary of photovoltaic performance of the best device shown in Fig. 2c

Scan mode	J_{SC} (mA cm^{-2})	V_{OC} (mV)	FF (%)	PCE (%)
Reverse	21.1	1100.1	68.9	16.0
Forward	19.2	1100.2	37.1	15.4

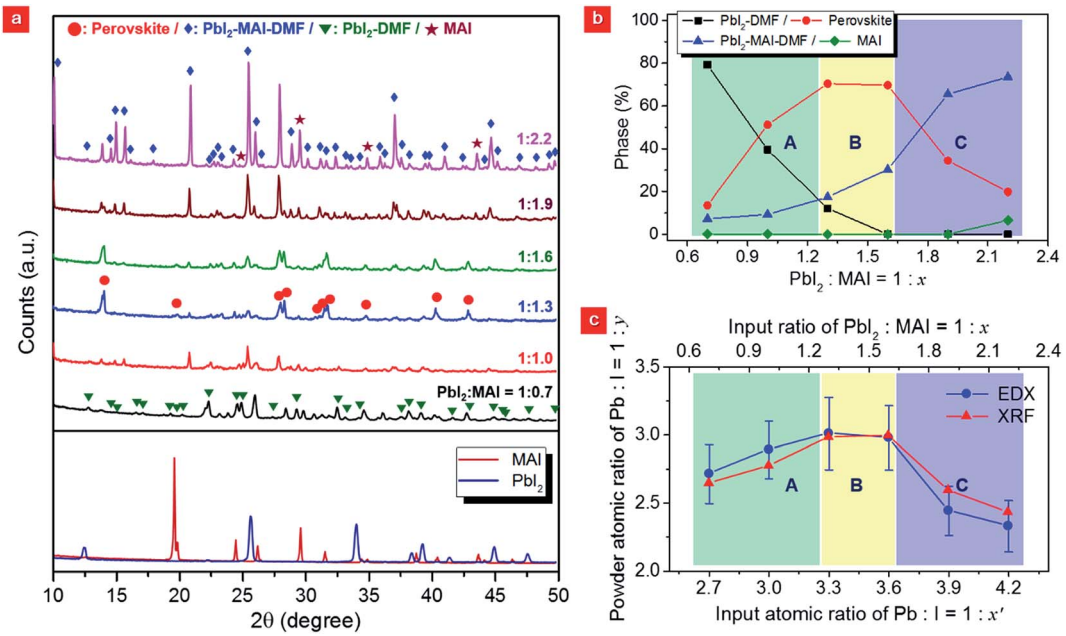

Fig. 3 Characterization of as-synthesized powders from different PbI_2 : MAI input ratios: (a) XRD patterns, (b) phase percentages, and (c) atomic ratios of Pb : I in the powders.

the percentage decreases sharply before reaching zero as the MAI ratio is increased. In contrast, with increasing MAI, the perovskite phase is remarkably increased until the ratio reaches 1 : 1.6; further increase in MAI corresponds to an abrupt decrease of perovskite. Simultaneously, the phase corresponding to the PbI_2–MAI–DMF complex is slowly increased until the ratio reaches 1 : 1.6, but it abruptly increases and becomes saturated with further increases in MAI.

Fig. 3c shows the atomic ratios of Pb : I obtained from energy-dispersive X-ray (EDX) and X-ray fluorescence (XRF) spectral analyses of the powders. Both spectra exhibit similar trends with ratio changes. The ratio of PbI_2 : MAI = 1 : x corresponds to the atomic ratio of Pb : I = 1 : (2 + x). We denote 2 + x as x' in the x axis of Fig. 3c to compare the input and output materials regarding the ratio of Pb : I. The output (*i.e.*, powder) ratio of Pb : I exhibits a trend similar to that of the input ratio until the ratio reaches 1 : 3. For Pb : I input ratios of 1 : >3, the output ratio is saturated at ~1 : 3 before abruptly decreasing. By comparing the results of Fig. 3b with c, we can deduce three points regarding the correlation between the PbI_2 : MAI input ratio and the phase formation of the output powders. First, the PbI_2–DMF complex is easily formed in PbI_2-excess conditions, as shown in the regions marked A in Fig. 3b and c. Second, an excess MAI amount of 30–50% is essential for perovskite phase formation, as shown in the regions marked B in Fig. 3b and c. Third, a large excess amount of MAI may assist in the formation of a stable PbI_2–MAI–DMF phase, but the excess is not consumed in forming this powder phase. Thus, I-deficient powders are synthesized at the ratios of 1 : 1.9 and 1 : 2.2 because of the presence of the stable PbI_2–MAI–DMF phase, despite the high input of excess MAI (regions labeled C in Fig. 3b and c).

We further investigated the structures and surface morphologies of the $MAPbI_3$ thin films fabricated using the phase-variable powders. The $MAPbI_3$ films were deposited under the same conditions used for those in the devices. Fig. 4a shows the typical XRD patterns of the $MAPbI_3$ thin films deposited on mp-TiO_2/TiO_2–BL/FTO. We find three expected phases of PbI_2, $MAPbI_3$, and FTO, from the patterns. To explore the phase variations depending on the input ratio, all XRD patterns are normalized with respect to the FTO peak intensity, permitting the comparison of the two phases of PbI_2 and $MAPbI_3$, as plotted in Fig. 4b. For the samples fabricated with PbI_2-excess conditions (region A of Fig. 4b), the PbI_2 phase is clearly observed in addition to the $MAPbI_3$ perovskite phase; its prevalence is decreased with increasing MAI. As the MAI ratio is further increased (regions B and C of Fig. 4b), the PbI_2 phase vanishes, and the $MAPbI_3$ phase gradually increases until reaching saturation. From these results with the powder analyses in Fig. 3, we can infer a strong correlation between the phases of the powders and structures of the final products. PbI_2 and $MAPbI_3$ structures are preferentially formed from the PbI_2–DMF–phase- and PbI_2–MAI–DMF-phase-dominant powders, respectively. These results suggest that the final structure can be controlled by tuning the phases of the precursor powders.

Fig. 4c shows the corresponding field-emission scanning electron microscope (FESEM) images of the film surface. The film fabricated with the powder having an input ratio of 1 : 0.7 exhibits small grains of <200 nm. Voids are visible in the film surface, as shown in the low-magnification FESEM image of Fig. S3.† As the MAI ratio is increased, the grain size becomes larger with an abrupt decrease of voids. A compact morphology without voids is obtained at the ratio of 1 : 1.6 (Fig. 4c and S3†). However, further MAI increases cause the re-appearance and increase in density of voids on the surface. These results indicate that the phases of the powders, as controlled by the input ratio, strongly affect the morphology of the final products, in

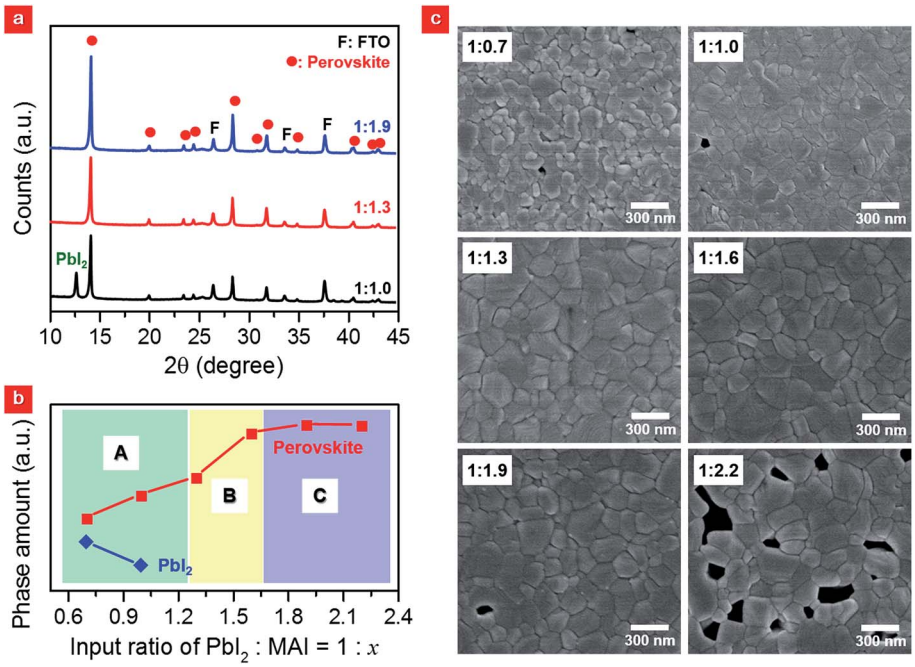

Fig. 4 (a) XRD patterns, (b) phase percentage, and (c) FESEM surface images of $MAPbI_3$ films deposited on mp-TiO_2/TiO_2–BL/FTO.

addition to the products' structures. Therefore, the best device performance obtained with the specific input ratio of PbI_2 : MAI = 1 : 1.6 (Fig. 2 and Tables 1 and 2) can be simply explained by the good crystallinity and uniform morphology of the film, associated with the optimal powder phase.

Based on these results, we propose a plausible explanation for the effects of the input ratio in fabricating the powder on the device performance. At the PbI_2-excess input condition (regions marked A in Fig. 3 and 4), the wide PbI_2 band-gap of 2.3 eV may obstruct charge transport and collection. The phase is preferentially formed in these conditions, as shown in Fig. 4a, and it may be evenly distributed over the film because a homogeneous precursor solution is used for film fabrication. The insufficient MAI also causes an incomplete $MAPbI_3$ phase formation with small average grain sizes,[14] as shown in Fig. 4c. Therefore, the device performance is poorer with PbI_2–DMF-phase-dominant powders. In the case of a large excess of MAI (regions marked C in Fig. 3 and 4), the samples exhibit the highest concentration of $MAPbI_3$ phase, but contain many voids on the film surface. These voids may cause decreased device performance because of the decreased light-harvesting and the undesirable direct contact between the HTM and the electron-transporting layer.[12] The void formation at high MAI excess conditions may be explained by the evaporation of unreacted MAI during the annealing process to form the $MAPbI_3$ film. The presence of MAI in the high-MAI-excess conditions (1 : 2.2) verifies this mechanism, as shown in XRD patterns (Fig. 3a and Table S1†). To further confirm this, we analyzed the film using Fourier-transform infrared (FT-IR) spectroscopy. As show in the spectrum of Fig. S4,† the MAI phase is clearly observed in addition to the PbI_2–MAI–DMF complex phase from the 1 : 2.2 powder, but is not present in the thin film fabricated using this powder. This indicates that the unreacted MAI, not involved in the formation of the PbI_2–MAI–DMF phase, is removed from the sample during film fabrication. Notably, no pure MAI phase is observed in the powder samples from input ratios of 1 : 0.7–1.6. Therefore, it can be deduced that the evaporation of unreacted MAI from the surface of the film during annealing leaves voids on the surface. In contrast to both PbI_2 and MAI excess conditions, the samples fabricated at moderate input ratio conditions (regions marked B in Fig. 3 and 4) exhibit good crystallinity and uniform morphology, which promote the best device performance.

Our method is similar to the previously reported, so-called 'one-step (solution or spin-coating) method',[13,14] from the perspective of single-step processing using a precursor solution. However, our method is fundamentally different from those previously used in terms of its technical features and the effects of input ratio. The main technical difference is that we synthesized phase-controlled powders before implementing them as chemical sources for perovskite deposition, rather than directly using a solution consisting of two mixed precursors at various molar ratios. This difference causes significant differences in the input ratio effects. In our method, the molar ratio determines the preferentially formed phase in the powder precursors, leading to a controlled structure and morphology of $MAPbI_3$ and thereby affecting device performance (Fig. 2–4). In the previous method, a controlled molar ratio influenced the nucleation and growth of $MAPbI_3$ because of the additive effect induced by an excess of either PbI_2 (ref. 15 and 16) or MAI.[13–15]

In addition to this technical difference, our method has four distinct advantages over the previous method. First, our method is less affected by the quality of the two starting chemicals (PbI_2 and MAI) in determining the device performance (Fig. S5†). In

previous reports, the presence of undesired materials in PbI_2 and MAI, such as impurities,[21] hydrated sources,[20] or stabilizers,[22] critically affected the device performances. This characteristic may be attributed to the exclusion of unnecessary substances from the assembly of a desired complex or crystal during step II, as drawn in Fig. 1. Second, our method can be extended to the formation of other hybrid perovskites, such as $MAPbBr_3$, $MAPbI_{3-x}Br_x$, and $FAPbI_3$, as shown in Fig. S6,† which supports the versatility of our method. Third, our method provides another effective solution for controlling the intermediate phase of hybrid perovskite materials. Many previous works have shown that intermediate phase formation is necessary to control the growth behaviors and morphology to ensure good device performance.[1,14,19] Typically, the intermediate phase has been controlled by either mixing two different solvents[1] or adding the proper amount of the desired solvent.[19] In our proposed method, the intermediate phases are controlled by modulating the input molar ratio (Fig. 2) or selecting appropriate polar solvents that easily dissolve $MAPbI_3$ (Fig. S7†). Finally, our devices exhibited greater efficiency and stability than those fabricated by the previous method (Fig. S8†). This may be explained by the low impurity of the $MAPbI_3$ solution for the spin coating, although further experiments and analysis are required to confirm this.

3. Conclusions

We have introduced an easy and versatile method based on phase-controlled powders for the fabrication of high-performance hybrid perovskite solar cells. Three phases corresponding to PbI_2–DMF complex, tetragonal $MAPbI_3$, and PbI_2–MAI–DMF complex were preferentially formed from powders having PbI_2-excess, moderate-ratio, and high excess MAI input conditions, respectively. The samples fabricated with powders having moderate ratio conditions of 1 : 1.3–1.9 exhibited uniform morphology and good crystallinity. As a result, the highest PCE of ~16% could be obtained from the optimum input ratio of 1 : 1.6. Our results demonstrate that the proposed approach is applicable and versatile in achieving high-performance hybrid perovskite solar cells.

4. Experimental section

Information on chemicals

Chemicals of various purities were purchased from different companies to verify reproducibility. PbI_2 with purities of 99% and 99.9985% were purchased from Sigma-Aldrich and Alfa Aesar, respectively. Hydroiodic acid (HI, 57 wt% in H_2O, 99.95%), DMF (anhydrous, 99.8%), chlorobenzene (99.8%), 4-*tert*-butylpyridine (*t*BP, 96%), bis(trifluoromethane)sulfonimide lithium salt (Li-TFSI, 99.95%), and acetonitrile (anhydrous, 99.8%) were purchased from Sigma-Aldrich. Ethyl alcohol (99.9%), diethyl ether (DE, extra pure grade), and DCM (extra pure grade) were purchased from Duksan (Korea). Methylamine (40% in methanol, *ca.* 9.8 mol L^{-1}) was purchased from TCI. Spiro-OMeTAD was purchased from 1-Material.

Synthesis of MAI

Prior to the synthesis of powders, the MAI was first synthesized by reacting 27.86 mL of methylamine and 30 mL of HI in a 250 mL round-bottom flask at 0 °C for 2 h with stirring. The HI was added dropwise to the methylamine solution at 0 °C to minimize impurity formation. White precipitates were obtained by the complete evaporation of the reacted solutions at 60 °C. Some of the as-obtained precipitates were recrystallized for purification by a two-solvent recrystallization technique, where ethanol and DE were used as solvents. Finally, the MAI was collected by a vacuum filtration technique and dried at 60 °C in vacuum for several days.

Synthesis and characterization of $MAPbI_3$ crystalline powders

For the synthesis of powders, various PbI_2 and MAI purities were used to verify the effects of the quality of starting chemicals. PbI_2 was used without further purification, but different PbI_2 sources of different purities were explored. For the MAI, the effects of the recrystallization (or purification) step were investigated. The synthetic procedure was briefly described in Fig. 1. All prepared powders were stored stably at ambient conditions for several months. Notably, the powders should be stored in a desiccator at room temperature. If they were stored at elevated temperatures of >50 °C, especially in vacuum, the DMF-including complexes could be easily broken so that the two phases of PbI_2–DMF and PbI_2–MAI–DMF could not be detected in the resulting products. This would cause misunderstanding of the powder phases. After preparation, the powders were characterized by XRD (Empyrean, PANalytical), FT-IR (Continuum, Thermo Scientific), and thermogravimetric analysis (Auto Q500, TA instruments).

Preparation of mp-TiO_2/TiO_2–BL/FTO substrate

Prior to deposition, the FTO (8 Ω square^{-1}, Pilkington) was first etched with Zn powder and HCl to obtain a desired electrode region. A thin compact TiO_2–BL of ~80 nm in thickness was then deposited on a pre-cleaned FTO using two repeated cycles of spin-coating with a 0.1 M TiO_2 sol–gel solution and subsequent drying at 200 °C. The TiO_2 precursor solution was synthesized by mixing two independent solutions: one was ethanol-based titanium(IV) isopropoxide (99.999%, Aldrich) and the other was HNO_3 (70%, Aldrich), de-ionized water, and ethanol. Then, the mp-TiO_2 with thickness ranges of 150–600 nm was deposited by spin-coating with a diluted TiO_2 paste solution (0.2 g mL^{-1} in ethanol, 20 nm diameter, Solaronix). The 200 nm-thick mp-TiO_2 layer was obtained by spin-coating at 7000 rpm for 30 s. Subsequently, the as-deposited samples were annealed at 500 °C in air for 2 h.

Fabrication and characterization of solar cells

The prepared powders (~45 wt%) were dissolved in DMF at room temperature to form the precursor solutions. Clear yellowish solutions were obtained after 1 h. The solutions were deposited on the mp-TiO_2/TiO_2–BL/FTO by spin-coating at 5000 rpm. In the course of spin-coating, a sufficient amount of

DE (~0.5 mL) was dripped onto the rotating substrates within a few seconds before the color was changed to white. Then the as-coated samples were annealed at 120 °C in air for 15 min. After the samples were cooled to room temperature, 80 μL of spiro-OMeTAD solution was deposited by spin-coating at 3000 rpm for 30 s. The spiro-OMeTAD solution was synthesized by dissolving 72.3 mg spiro-OMeTAD, 17.5 μL Li-TFSI solution (520 mg mL^{-1} in acetonitrile), and 28.8 μL tBP in 1 mL chlorobenzene. Finally, a Au electrode of ~70 nm was deposited by a thermal evaporator.

Characterization of $MAPbI_3$ and solar cells

The morphology, crystal structure, surface, and absorption properties of $MAPbI_3$ were characterized by FE-SEM (S-4800, Hitachi), XRD, FT-IR, and UV-Vis absorption spectroscopy (CARY5000, Agilent), respectively. The *J–V* curves were measured with a metal mask of 0.096 cm^2 in area using a source meter (2400, Keithley) unit and a solar simulator (94022A, Newport) to simulate 1.5G solar irradiation (100 mW cm^{-2}). The light intensity was adjusted by a Si-reference cell certificated by NREL before measurements.

Acknowledgements

This work was supported by the DGIST R&D Program of the Ministry of Science, ICT and Technology of Korea (16-EN-03).

References

1 N. J. Jeon, J. H. Noh, Y. C. Kim, W. S. Yang, S. Ryu and S. I. Seok, *Nat. Mater.*, 2014, **13**, 897–903.
2 W. S. Yang, J. H. Noh, N. J. Jeon, Y. C. Kim, S. Ryu, J. Seo and S. I. Seok, *Science*, 2015, **348**, 1234–1237.
3 D. P. McMeekin, G. Sadoughi, W. Rehman, G. E. Eperon, M. Saliba, M. T. Hörantner, A. Haghighirad, N. Sakai, L. Korte and B. Rech, *Science*, 2016, **351**, 151–155.
4 M. Saliba, T. Matsui, J.-Y. Seo, K. Domanski, J.-P. Correa-Baena, M. K. Nazeeruddin, S. M. Zakeeruddin, W. Tress, A. Abate and A. Hagfeldt, *Energy Environ. Sci.*, 2016, **9**, 1989–1997.
5 C. Yi, X. Li, J. Luo, S. M. Zakeeruddin and M. Grätzel, *Adv. Mater.*, 2016, **28**, 2964–2970.
6 M. Ye, X. Hong, F. Zhang and X. Liu, *J. Mater. Chem. A*, 2016, **4**, 6755–6771.
7 T. A. Berhe, W.-N. Su, C.-H. Chen, C.-J. Pan, J.-H. Cheng, H.-M. Chen, M.-C. Tsai, L.-Y. Chen, A. A. Dubale and B.-J. Hwang, *Energy Environ. Sci.*, 2016, **9**, 323–356.
8 N. K. Noel, S. D. Stranks, A. Abate, C. Wehrenfennig, S. Guarnera, A.-A. Haghighirad, A. Sadhanala, G. E. Eperon, S. K. Pathak and M. B. Johnston, *Energy Environ. Sci.*, 2014, **7**, 3061–3068.
9 H. J. Snaith, A. Abate, J. M. Ball, G. E. Eperon, T. Leijtens, N. K. Noel, S. D. Stranks, J. T.-W. Wang, K. Wojciechowski and W. Zhang, *J. Phys. Chem. Lett.*, 2014, **5**, 1511–1515.
10 B. Chen, M. Yang, S. Priya and K. Zhu, *J. Phys. Chem. Lett.*, 2016, **7**, 905–917.
11 W. Chen, Y. Wu, J. Liu, C. Qin, X. Yang, A. Islam, Y.-B. Cheng and L. Han, *Energy Environ. Sci.*, 2015, **8**, 629–640.
12 L. Zheng, D. Zhang, Y. Ma, Z. Lu, Z. Chen, S. Wang, L. Xiao and Q. Gong, *Dalton Trans.*, 2015, **44**, 10582–10593.
13 Y. Zhou, O. S. Game, S. Pang and N. P. Padture, *J. Phys. Chem. Lett.*, 2015, **6**, 4827–4839.
14 A. Sharenko and M. F. Toney, *J. Am. Chem. Soc.*, 2015, **138**, 463–470.
15 Z. Song, S. C. Watthage, A. B. Phillips, B. L. Tompkins, R. J. Ellingson and M. J. Heben, *Chem. Mater.*, 2015, **27**, 4612–4619.
16 C. Roldán-Carmona, P. Gratia, I. Zimmermann, G. Grancini, P. Gao, M. Graetzel and M. K. Nazeeruddin, *Energy Environ. Sci.*, 2015, **8**, 3550–3556.
17 G. Li, T. Zhang and Y. Zhao, *J. Mater. Chem. A*, 2015, **3**, 19674–19678.
18 W. Zhang, M. Saliba, D. T. Moore, S. K. Pathak, M. T. Hörantner, T. Stergiopoulos, S. D. Stranks, G. E. Eperon, J. A. Alexander-Webber and A. Abate, *Nat. Commun.*, 2015, **6**, 6142.
19 N. Ahn, D.-Y. Son, I.-H. Jang, S. M. Kang, M. Choi and N.-G. Park, *J. Am. Chem. Soc.*, 2015, **137**, 8696–8699.
20 A. Wakamiya, M. Endo, T. Sasamori, N. Tokitoh, Y. Ogomi, S. Hayase and Y. Murata, *Chem. Lett.*, 2014, **43**, 711–713.
21 J. Chang, H. Zhu, B. Li, F. H. Isikgor, Y. Hao, Q. Xu and J. Ouyang, *J. Mater. Chem. A*, 2016, **4**, 887–893.
22 Z. Xiao, D. Wang, Q. Dong, Q. Wang, W. Wei, J. Dai, X. Zeng and J. Huang, *Energy Environ. Sci.*, 2016, **9**, 867–872.
23 D. Shi, V. Adinolfi, R. Comin, M. Yuan, E. Alarousu, A. Buin, Y. Chen, S. Hoogland, A. Rothenberger and K. Katsiev, *Science*, 2015, **347**, 519–522.
24 X. Guo, C. McCleese, C. Kolodziej, A. C. Samia, Y. Zhao and C. Burda, *Dalton Trans.*, 2016, **45**, 3806–3813.